

Cite this: *Chem. Sci.*, 2020, 11, 5487

All publication charges for this article have been paid for by the Royal Society of Chemistry

## Vibrational characterization of a diiron bridging hydride complex – a model for hydrogen catalysis†

Leland B. Gee,<sup>†a</sup> Vladimir Pelmentschikov,<sup>†\*b</sup> Hongxin Wang,<sup>†c</sup> Nakul Mishra,<sup>†d</sup> Yu-Chiao Liu,<sup>†ef</sup> Yoshitaka Yoda,<sup>g</sup> Kenji Tamasaku,<sup>h</sup> Ming-Hsi Chiang<sup>†\*ef</sup> and Stephen P. Cramer<sup>†\*c</sup>

A diiron complex containing a bridging hydride and a protonated terminal thiolate of the form  $[(\mu, \kappa_2\text{-bdTH})(\mu\text{-PPh}_2)(\mu\text{-H})\text{Fe}_2(\text{CO})_5]^+$  has been investigated through  $^{57}\text{Fe}$  nuclear resonance vibrational spectroscopy (NRVS) and interpreted using density functional theory (DFT) calculations. We report the  $\text{Fe}\text{-}\mu\text{H}\text{-Fe}$  wagging mode, and indications for  $\text{Fe}\text{-}\mu\text{D}$  stretching vibrations in the D-isotopologue, observed by  $^{57}\text{Fe}$ -NRVS. Our combined approach demonstrates an asymmetric sharing of the hydride between the two iron sites that yields two nondegenerate  $\text{Fe}\text{-}\mu\text{H/D}$  stretching vibrations. The studied complex provides an important model relevant to biological hydrogen catalysis intermediates. The complex mimics proposals for the binuclear metal sites in  $[\text{FeFe}]$  and  $[\text{NiFe}]$  hydrogenases. It is also an appealing prototype for the 'Janus intermediate' of nitrogenase, which has been proposed to contain two bridging  $\text{Fe}\text{-H}\text{-Fe}$  hydrides and two protonated sulfurs at the  $\text{FeMo}$ -cofactor. The significance of observing indirect effects of the bridging hydride, as well as obstacles in its direct observation, is discussed in the context of biological hydrogen intermediates.

Received 2nd March 2020

Accepted 1st May 2020

DOI: 10.1039/d0sc01290d

rsc.li/chemical-science

## Introduction

Biological hydrogen catalysis is driven by a ubiquitous and diverse set of enzymes called hydrogenases<sup>1–4</sup> and to a lesser extent by the nitrogenase family.<sup>5</sup> Hydrogenases reversibly convert molecular hydrogen into reducing power at binuclear  $[\text{FeFe}]$ , binuclear  $[\text{NiFe}]$ ,<sup>6</sup> or mononuclear  $[\text{Fe}]$  active sites.<sup>7</sup> Similarly, hydrogen evolution in Mo-nitrogenase occurs at a unique  $\text{Fe}_7\text{MoS}_9\text{C}$  cluster called the  $\text{FeMo}$ -cofactor, and analogous chemistry likely occurs at the  $\text{Fe(V,Fe)}$ -cofactors.<sup>8,9</sup> The activities of all these enzymes are presumably related by the

formation of metastable  $\text{Fe}\text{-H}^-$  hydrides and protonation of nearby sulfurs during catalysis (Fig. 1).<sup>6,10,11</sup> Synthesis and characterization of model complexes that can simulate biochemical intermediates and their proton transfer capabilities by the stabilization of transition metal hydrides ( $\text{M}\text{-H}^-$ ) and nearby thiols ( $\text{-SH}$ ) are key to understanding hydrogenase and nitrogenase active site hydrogen catalysis.<sup>10,12–16</sup>

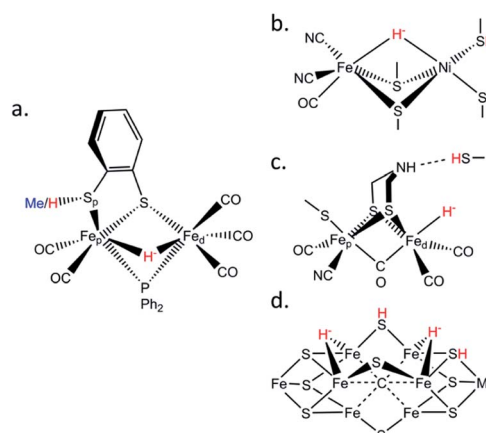


Fig. 1 Schematic structures of (a) the  $\mu\text{HS}(\text{Me}/\text{H})$  synthetic complexes studied in this work; (b) the  $[\text{NiFe}]$  hydrogenase Ni-R intermediate; (c) the  $[\text{FeFe}]$  hydrogenase  $\text{H}_{\text{hyd}}$  intermediate; (d) the nitrogenase Janus intermediate. The iron hydrides and sulfur protonations are labelled in red.

<sup>a</sup>Department of Chemistry, Stanford University, 333 Campus Drive, Stanford, CA 94305, USA

<sup>b</sup>Institut für Chemie, Technische Universität Berlin, Strasse des 17 Juni 135, 10623 Berlin, Germany. E-mail: pelmentschikov@tu-berlin.de

<sup>c</sup>SETI Institute, 189 Bernardo Avenue, Mountain View, CA 94043, USA. E-mail: scramer@seti.org

<sup>d</sup>Department of Chemistry, University of California, Davis, One Shields Ave, Davis, CA 95616, USA

<sup>e</sup>Institute of Chemistry, Academia Sinica, Nankang, Taipei 115, Taiwan

<sup>f</sup>Department of Medicinal and Applied Chemistry, Kaohsiung Medical University, Kaohsiung 807, Taiwan

<sup>g</sup>Japan Synchrotron Radiation Research Institute (JASRI), Spring-8, 1-1-1 Kouto, Sayo-gun, Hyogo 679-5198, Japan

<sup>h</sup>RIKEN Spring-8 Center, 1-1-1 Kouto, Sayo-cho, Sayo-gun, Hyogo 679-5148, Japan

† Electronic supplementary information (ESI) available: Materials and methods, Fig. S1–S12, Table S1, atomic Cartesian coordinates, animated vibrational modes. See DOI: 10.1039/d0sc01290d

‡ These authors contributed equally.



These special  $-SH/M-H^-$  interactions take various forms. In [FeFe] hydrogenases there is a conserved cysteine situated at the end of a proton transfer chain formed by hydrophilic amino acid residues and water molecules, with the  $-SH$  thiol group adjacent to an azadithiolate (ADT) bridge of the  $[2Fe]_H$  sub-cluster (Fig. 1c). There is considerable evidence that the ADT bridge plays a critical role in proton acceptance and relay to the catalytic  $Fe_d$  site.<sup>17</sup> Moreover, disruption of the proton supply chain in the enzymes from *Chlamydomonas reinhardtii* (CrHydA1) or *Desulfovibrio desulfuricans* (DdHydAB) has allowed the transient  $H_{hyd}$  catalytic state to be trapped and unequivocally shown to involve a terminal  $Fe_d-H^-$  hydride (Fig. 1c).<sup>14,18-21</sup> For [NiFe] hydrogenases, the catalytic Ni-R state has been shown to feature a bridging hydride, with a Ni-bound protonated cysteine sulfur (Fig. 1b).<sup>6</sup> Finally, in nitrogenases the  $E_2$  state is presumed to have one bridging  $Fe-H^-$ -Fe hydride with a nearby protonated sulfur capable of  $H_2$  release, while two hydrides capable of reductive elimination have been proposed for the  $E_4$  or 'Janus intermediate' of the Fe(Mo,V,Fe)-cofactor (Fig. 1d).<sup>9</sup>

To model the aforementioned biological hydrides, previous efforts produced and characterized synthetic protonated thiols coordinated to diiron centers.<sup>22-25</sup> Here we extend this work by exploring  $^{57}Fe$ -specific vibrational dynamics for a diiron center with a bridging hydride and a protonated thiol ligand. Specifically, we have characterized the  $[(\mu, \kappa_2\text{-bdtH})(\mu\text{-PPh}_2)(\mu\text{-H})Fe_2(CO)_5]^+$  (bdt = 1,2-benzenedithiolate) model compound, referred hereafter as ' $\mu\text{HSH}$ ' (Fig. 1a), and as well its deuterated isotopologue  $[(\mu, \kappa_2\text{-bdtD})(\mu\text{-PPh}_2)(\mu\text{-D})Fe_2(CO)_5]^+$ ,  $\mu\text{DSD}$ , using nuclear resonance vibrational spectroscopy (NRVS). We also recorded the spectrum of the *S*-methylated complex:  $[(\mu, \kappa_2\text{-bdtCH}_3)(\mu\text{-PPh}_2)(\mu\text{-H})Fe_2(CO)_5]^+$ , here referred to as ' $\mu\text{HSMe}$ '.

$^{57}Fe$ -NRVS is a synchrotron-based technique that observes excitation of an  $^{57}Fe$  nucleus together with the excitation/deexcitation of vibrational modes.<sup>26-28</sup> NRVS is essentially the recoil fraction that steals intensity from the recoil-free Mössbauer effect, with the measured intensity for a given

normal mode proportional to the  $^{57}Fe$  kinetic energy in that mode, ultimately yielding an  $^{57}Fe$  partial vibrational density of states (PVDOS). The experimental frequencies and intensities can be directly compared with normal mode calculations from density functional theory (DFT) or even empirical force fields.

The asymmetric diferrous compound  $\mu\text{HSH}$  is relevant to the protonated and bridging hydride-bound states proposed for  $H_2$  production in [NiFe] hydrogenases and to the nitrogenase  $E_2$  and  $E_4$  intermediates. It is also a good benchmark for comparison with the NRVS for intermediates in [FeFe] hydrogenase proposed to contain a  $\mu$ -hydride ligand bridging the  $Fe_p(\text{II})$  and  $Fe_d(\text{II})$  sites (Fig. S1†).<sup>29</sup> In line with a recent interpretation that [FeFe] hydrogenase operates exclusively with bridging CO intermediates,<sup>30</sup> the  $\mu$ -hydride intermediates were attributed to the enzyme's 'slow cycle'.

## Results

### NRVS spectra and qualitative assignments

The overall NRVS-derived  $^{57}Fe$ -PVDOS for the  $\mu\text{HSH}$ ,  $\mu\text{DSD}$  and  $\mu\text{HSMe}$  samples are compared in Fig. 2. Qualitative assignments can be made based on comparison with previous spectra for Fe-S proteins and model compounds. The low energy  $<200\text{ cm}^{-1}$  portion of the spectrum is related to acoustic and torsional modes largely involving the bulky Ph and bdt subunits, as well as bending modes at the Fe sites. The next region up to  $400\text{ cm}^{-1}$  comprises predominantly Fe-S and Fe-P stretching modes. The  $400\text{--}650\text{ cm}^{-1}$  region has prominent features from modes that are a mix of  $\nu\text{Fe-CO}$  stretching and  $\delta\text{Fe-CO}$  bending.

At higher energies, a band at  $745\text{ cm}^{-1}$  is particularly significant – it represents an Fe-H-Fe wagging mode. This assignment is based on comparison with results for similar Fe- $\mu\text{H}^-$ -Fe synthetic complexes and their computational models,<sup>31,32</sup> as well as Ni- $\mu\text{H}^-$ -Fe models and the Ni-R state of [NiFe] hydrogenase.<sup>11</sup> The significant weakening at this position in the  $\mu\text{DSD}$  spectrum supports this assignment; residual

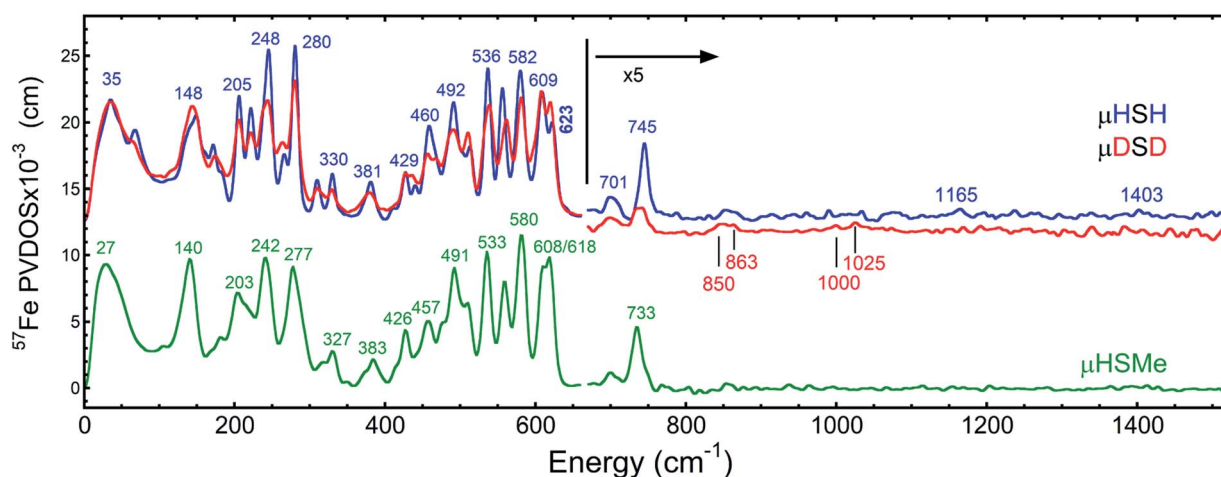


Fig. 2 Top: the NRVS-derived  $^{57}Fe$ -PVDOS spectra for  $\mu\text{HSH}$  (—) and its deuterium isotopologue  $\mu\text{DSD}$  (—), vertically offset by  $1 \times 10^{-3}\text{ cm}$  from each other in the high-energy region. Bottom: the  $^{57}Fe$ -PVDOS spectra for  $\mu\text{HSMe}$  (—). In all cases the high-energy region intensity above  $650\text{ cm}^{-1}$  is multiplied by 5 for visibility. The bands are labelled with their top positions, with those above  $800\text{ cm}^{-1}$  assigned tentatively.



intensity likely results from an incomplete H-to-D exchange. Below the  $745\text{ cm}^{-1}$  band is a second candidate wagging mode feature at  $\sim 701\text{ cm}^{-1}$ . Although this energy region coincides with benzene-dithiol modes, their Fe motion is predicted to be low. The energy is also consistent with the predicted hydride wagging motion of a deprotonated species,  $\mu\text{HS}^-$ , based on DFT calculations as described below. For the  $\mu\text{HSMe}$  complex, a slight downshift to  $733\text{ cm}^{-1}$  is observed for the main wagging mode feature.

From previous NRVS work on Fe-H/D<sup>-</sup> complexes,<sup>11,31,32</sup> as well as guidance from the conventional vibrational spectroscopy literature,<sup>33</sup> we expect observation of the Fe-H stretching modes at vibrational energies above  $1100\text{ cm}^{-1}$ . There are hints of such features at  $1165\text{ cm}^{-1}$  and  $1403\text{ cm}^{-1}$ , but the signal-to-noise is not convincing. Even in the best of cases, these modes are extremely weak in NRVS because they primarily involve the hydride nucleus motion with an almost static Fe partner. Below, we will use DFT calculations to investigate additional factors such as sample heterogeneity and intermolecular coupling that conspire to split the already weak Fe-H stretches into a multitude of even weaker modes that are below the current detection limit.

### DFT calculations and quantitative comparisons

The  $^{57}\text{Fe}$ -PVDOS predictions from the DFT models for  $\mu\text{HSH}$ ,  $\mu\text{DSD}$ , and  $\mu\text{HSMe}$  (Fig. S3a and S4†) are compared in Fig. 3, S8 and S9.† The key experimental feature at  $745\text{ cm}^{-1}$ , attributed to the Fe-H-Fe wagging mode, is reproduced very well in terms of energy and intensity by the calculated band at  $746\text{ cm}^{-1}$ . In this mode, the calculated  $\mu\text{H}^-$  hydride motion is normal to the 'Fe-H-Fe' plane, as shown in Fig. S5 (see additionally ESI for animated vibrational modes, and Fig. S8 for an overlay of the NRVS-observed and DFT-predicted spectra).† A corresponding Fe-D-Fe wagging is not specifically resolved in the NRVS of the deuterated sample.

To better understand the differences in these two spectra, we calculated the PVDOS for the bridging H and D nuclei, as shown in Fig. 4 and S7d.† Inspection of these curves reveals three distinct hydride bands, whereas there are only two distinct deuteride bands above  $650\text{ cm}^{-1}$ . The intensity for the third deuteride band (corresponding to the wagging motion) is redistributed throughout the  $400\text{--}600\text{ cm}^{-1}$  region, indicating significant coupling in the motions of the D nucleus with the five CO ligands. A comparison of the single wagging mode in  $\mu\text{HSH}$  with three prominent  $\mu\text{DSD}$  modes involving coupled motions is also depicted in Fig. S5.†

The computed spectrum of  $\mu\text{DSD}$  sees shifts of the Fe-H stretching modes at  $1424/1196\text{ cm}^{-1}$  to respectively  $1015/855\text{ cm}^{-1}$ . The  $^{57}\text{Fe}$ -PVDOS intensities of the Fe-D (vs. Fe-H) bands are enhanced due to the amplified  $^{57}\text{Fe}$  displacements when the heavier deuteride is the bridging ligand, which allows the Fe-D stretching signals to raise above the NRVS noise level (Fig. S11 and S12†). For future NRVS observation of such stretching modes, Fe-D complexes are clearly favored over Fe-H isotopologues.

### Asymmetric hydride sharing by Fe<sub>p</sub> and Fe<sub>d</sub>

We also calculated separate PVDOS for the  $^{57}\text{Fe}_p$  and  $^{57}\text{Fe}_d$  nuclei, as shown in Fig. 4 and S7c.† We use this notation for the Fe sites respectively proximal and distal to the thiol, following the notation commonly employed for [FeFe] hydrogenases, see Fig. 1 and S1.† Although both Fe atoms contribute to the vibrational motion, we can discriminate between the two Fe<sub>p/d</sub>- $\mu\text{H}$  stretching modes by the Fe-H bond that aligns closest to the  $\mu\text{H}$  displacement vector, as shown in Fig. S6 and visualized in the ESI† animations. Breakdown of the DFT  $^{57}\text{Fe}$ -PVDOS into individual  $^{57}\text{Fe}_{p/d}$  contributions demonstrates that the Fe-H modes are asymmetrically comprised of mostly the Fe<sub>d</sub> motion. The Fe<sub>d</sub>- $\mu\text{H}$  stretching mode is predicted for the high-end of the  $\mu\text{HSH}$  spectrum at  $1424\text{ cm}^{-1}$ , while the predicted Fe<sub>p</sub>- $\mu\text{H}$

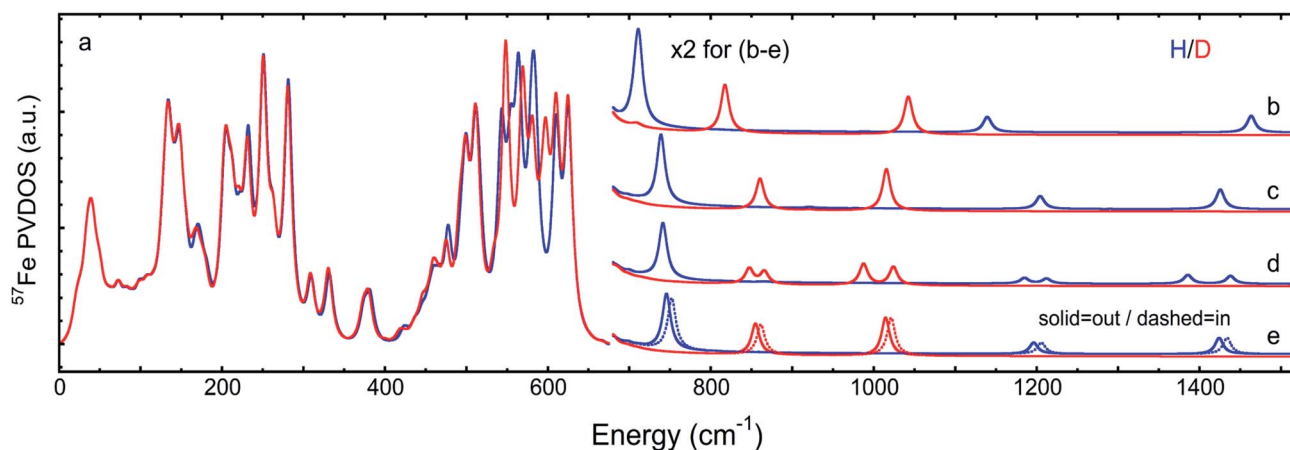


Fig. 3 DFT-based  $^{57}\text{Fe}$ -PVDOS for different chemical models and their isomers. Left (a):  $\mu\text{HSH}$  or  $\mu\text{DSD}$ . Right, top to bottom: (b)  $\mu\text{HS}^-$  or  $\mu\text{DS}^-$ , (c)  $\mu\text{HSMe}_{\text{in}}$  or  $\mu\text{DSMe}_{\text{in}}$ , (d)  $[\mu\text{HSH}]_2$  or  $[\mu\text{DSD}]_2$ , (e)  $\mu\text{HSH}_{\text{in}}$  vs.  $\mu\text{HSH}$  ( $=\mu\text{HSH}_{\text{out}}$ ) or  $\mu\text{DSD}_{\text{in}}$  vs.  $\mu\text{DSD}$  ( $=\mu\text{DSD}_{\text{out}}$ ). The high energy region  $>650\text{ cm}^{-1}$  (b–e) is multiplied by 2 for visibility. In (a), the intensities  $<210\text{ cm}^{-1}$  are based on the  $[\mu\text{HSH}]_2$  or  $[\mu\text{DSD}]_2$  dimer calculations, as explained in the main text and shown in Fig. 5.



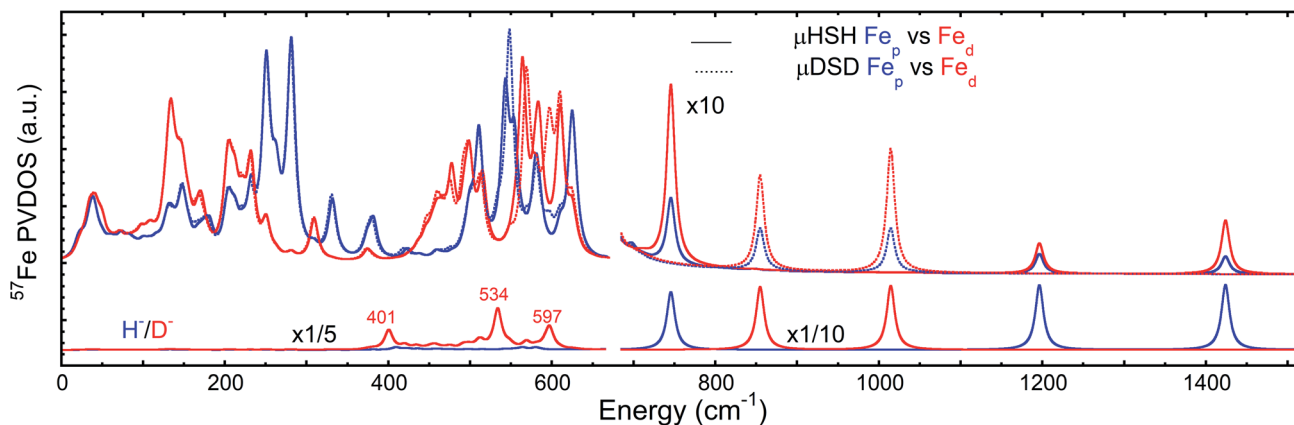


Fig. 4 Top: comparison of DFT-predicted  $^{57}\text{Fe}_d$  and  $^{57}\text{Fe}_p$  PVDOS for models  $\mu\text{HSH}$  and  $\mu\text{DSD}$ . Bottom: comparison of DFT-predicted  $\mu\text{H/D}$  PVDOS for the same models. The relative intensity multiplication factors ( $\times$ ) are applied for visibility.

stretch is at a lower energy of  $1196\text{ cm}^{-1}$ . Experimentally these hydride modes coincide with intensities at  $1403$  and  $1165\text{ cm}^{-1}$  respectively (Fig. 2 and S7 $\dagger$ ), however the signal-to-noise is low for these features despite several long acquisition experiments at high incident flux (see ESI Methods $\dagger$ ). On the other hand, the two most intense experimental bands at  $245/280\text{ cm}^{-1}$  (Fig. 2) are reproduced by DFT at  $251/281\text{ cm}^{-1}$  (Fig. S7 $\dagger$ ) and identified as mostly  $\text{Fe}_p\text{-S/P}$  stretching in character – the quantitative agreement with the NRVS experiment indicates a proper modeling of the electronic structure by a low-spin  $2\text{Fe(II)}$  core, also consistent with the recorded Mössbauer spectrum, see Fig. S2 and ESI Discussion. $\dagger$

The deduction that the  $\text{Fe}_d$  site contributes more NRVS intensity than the  $\text{Fe}_p$  site in the wagging and stretching hydride modes is supported by the differing Fe–H bond lengths revealed in the DFT-optimized geometry of  $\mu\text{HSH}$ ,  $\text{Fe}_p\text{-H} = 1.73\text{ \AA}$  vs.  $\text{Fe}_d\text{-H} = 1.65\text{ \AA}$ ; comparable values and their variations are seen as well in the X-ray structure<sup>34</sup> (Table S1 $\dagger$ ). The  $\sim 0.1\text{ \AA}$  difference in the  $\text{Fe}_{p/d}\text{-H}$  bond lengths as well rationalizes the  $\sim 230$  and  $\sim 160(\sim 230/\sqrt{2})\text{ cm}^{-1}$  splittings in the predicted  $\text{Fe}_{p/d}\text{-}\mu\text{H}$  and  $\text{Fe}_{p/d}\text{-}\mu\text{D}$  stretching frequencies.

### Conformational heterogeneity of the Fe thiol

We also considered the possibility of alternate structural conformations having an effect on the NRVS profiles. We found from DFT calculations that a local minimum was produced by reorientation of the protonated  $\text{S}_p\text{-H}_s$  thiolate ligand of  $\text{Fe}_p$  towards the bridging hydride, yielding a ' $\mu\text{HSH}_{\text{in}}$ ' (or ' $\mu\text{DSD}_{\text{in}}$ ') structure (Fig. S3a $\dagger$ ). The calculated energy difference was a trivial  $+0.3\text{ kcal mol}^{-1}$  compared to the above described best-fit model having the  $\text{S}_p\text{-H}_s$  moiety oriented away from the hydride, referred to simply as  $\mu\text{HSH}$  (or  $\mu\text{DSD}$ ). We thus expect  $\mu\text{HSH}$  ( $=\mu\text{HSH}_{\text{out}}$ ) and  $\mu\text{HSH}_{\text{in}}$  species to reach an equilibrium and co-exist in the sample crystals. The calculated  $^{57}\text{Fe}$ -PVDOS for  $\mu\text{HSH}_{\text{in}}$  produced an Fe–H–Fe wag at  $752\text{ cm}^{-1}$ , upshifted by  $6\text{ cm}^{-1}$  from the spectrum for  $\mu\text{HSH}$  (Fig. 3 and S8 $\dagger$ ). Slightly larger upshifts of  $7\text{ cm}^{-1}$  and  $10\text{ cm}^{-1}$  were predicted for the Fe–D and Fe–H stretching modes, respectively.

### Chemical heterogeneity of the Fe thiolate

From previous work with this compound, we know that deprotonation of the  $\text{S}_p\text{-H}_s$  moiety occurs readily (for example, upon solvation of  $\mu\text{HSH}$  in THF), and we refer to the resultant thiolate species as ' $\mu\text{HS}^-$ ' (Fig. S3a $\dagger$ ). DFT calculations on this candidate predict a  $35\text{ cm}^{-1}$  red-shift in the Fe–H–Fe wagging mode to  $711\text{ cm}^{-1}$  (Fig. S8b $\dagger$ ). The  $\mu\text{HS}^-$  model is thus a possible explanation for the weak feature observed at  $\sim 701\text{ cm}^{-1}$  in the experimental spectrum of  $\mu\text{HSH}$  – although a similar, but weaker, feature was observed in  $\mu\text{HSMc}$ , implying the source of this intensity need not be limited to the  $\mu\text{HS}^-$  species in the spectrum of  $\mu\text{HSH}$  (Fig. 2, S7a, and S9 $\dagger$ ).

An even higher degree of hydride sharing asymmetry is calculated for the  $\mu\text{HS}^-/\mu\text{DS}^-$  model (Table S1 $\dagger$ ) and, consequently, larger energy splittings between the predicted bands for the  $\text{Fe}_{p/d}\text{-}\mu\text{H/D}$  stretches (Fig. 3b and S8b $\dagger$ ). Specifically, the  $\text{Fe}_p\text{-}\mu\text{H/D}$  stretches calculated respectively at  $818/1138\text{ cm}^{-1}$  are significantly red-shifted when compared to the best-fit  $\mu\text{HSH}/\mu\text{DSD}$  model, due to a stronger  $\text{Fe}_p\text{-S}_p$  bond strength which in turn leads to a weaker adjacent  $\text{Fe}_p\text{-}\mu\text{H}^-$  bonding. Notably, the deprotonation of  $\mu\text{HSH}$  to  $\mu\text{HS}^-$  leads to a predicted upshift by  $15\text{ cm}^{-1}$  ( $332$  to  $347\text{ cm}^{-1}$ , Fig. S8b $\dagger$ ) for the band observed at  $330\text{ cm}^{-1}$  and having the strongest  $\text{Fe}_p\text{-S}_p$  stretching character (see ESI $\dagger$  for these modes animated). Finally, to produce a more realistic simulation of the observed NRVS spectrum, in Fig. 6 and S12 $\dagger$  we provide an average of the three DFT models considered above.

### Intermolecular coupling – the dimer model

A common weakness of DFT simulations of the NRVS spectra of solids is the lack of predicted intensity in the low-energy regions ( $<100\text{ cm}^{-1}$ ). In solid model complexes, the experimental modes in this region are due to solid matrix motions, and lattice or acoustic modes. In larger biological samples, this energy region corresponds primarily to torsional/dihedral modes and larger scale motions of the protein, and it provides an indicator of coupling between the motion of the  $^{57}\text{Fe}$ -enriched bioinorganic core and its environment.<sup>18,20,35,36</sup> To partially account for these modes in our calculations, we have used a DFT model based on



a dimeric form  $[\mu\text{HSH}]_2$  which is directly available from the crystallographic unit cell in the X-ray structure (Fig. S3b<sup>†</sup>);<sup>34</sup> this approach is justified as the NRVS experiment employed a polycrystalline powder sample.

The vibrational calculation on  $[\mu\text{HSH}]_2$  shows an increased density of normal modes and significant improvement in the

low-energy  $<200\text{ cm}^{-1}$  region of the predicted NRVS spectrum over that of the  $\mu\text{HSH}$  monomer only (Fig. 5 and S10<sup>†</sup>). Of note is reproduction of the broad experimental feature centered at  $35\text{ cm}^{-1}$  produced by highly-delocalized expansions of the dimer, see Fig. 5 and ESI<sup>†</sup> for the representative normal mode at  $38\text{ cm}^{-1}$  animated. The intermolecular dispersion interaction plays an important role here, included as a correction to our DFT setup on  $[\mu\text{HSH}]_2$  (see ESI Methods<sup>†</sup>). The dimer computational model does not capture all of the features in the low-energy region – specifically the prominence at  $\sim 70\text{ cm}^{-1}$  – which may be reproduced by models accounting for more molecules and/or their structural periodicity, however such a computational effort is beyond the scope of this work.

Notably, the dimer is composed of  $\mu\text{HSH}$  and its mirror-image isomer  $\mu\text{HSH}_m$ , or the enantiomer, yet the  $[\mu\text{HSH}]_2$  structure itself does not exhibit a symmetry (higher than  $C_1$ ). Deviation from the exact mirror-image symmetry between  $\mu\text{HSH}$  and  $\mu\text{HSH}_m$  effectively splits the Fe– $\mu\text{H/D}$  stretching normal modes  $>800\text{ cm}^{-1}$ , which are particularly sensitive to even minimal Fe– $\mu\text{H}$  bond length changes of  $\sim 0.01\text{ \AA}$  (Table S1<sup>†</sup>), in line with the hydride mode variations indicated above for the monomer models. This results in a more faithful simulation of their low PVDOS intensities – see the calculated  $[\mu\text{HSH}]_2/[\mu\text{DSD}]_2$  vs.  $\mu\text{HSH}/\mu\text{DSD}$  spectra compared to the observed H/D sample NRVS data in Fig. 6, S10, and S12.<sup>†</sup>

## Discussion

Our results on the bridging hydride samples show both the strengths and limitations of NRVS for observation of Fe–H normal modes. The experimental and calculated observations demonstrate that the Fe–H–Fe wag mode is sensitive to the chemistry at the Fe–S ligand, reflected by the species-dependent redistribution of intensity in the  $690\text{--}760\text{ cm}^{-1}$  region. The DFT calculations suggest the wag mode is even sensitive to the conformation of the SH proton, shifting  $6\text{ cm}^{-1}$  between the ‘in’ and ‘out’ conformers. In the range of the models considered,  $\sim 40\text{ cm}^{-1}$  upshift of the predicted wag band position is approximately correlated with

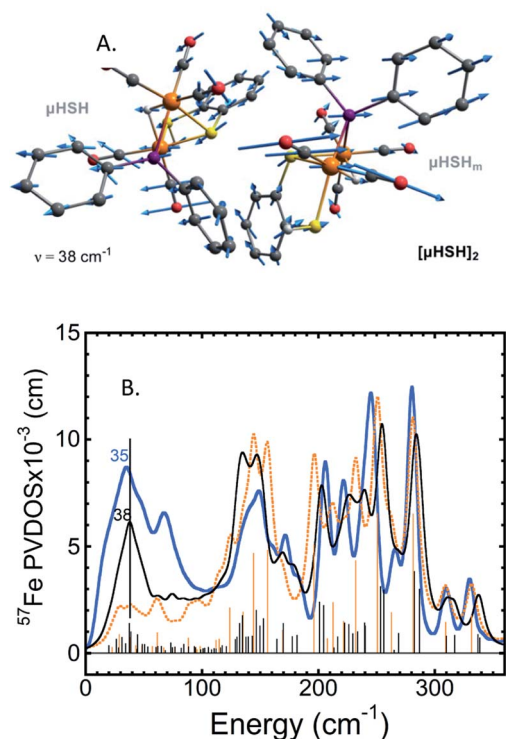


Fig. 5 (A) The normal mode calculated at  $38\text{ cm}^{-1}$  showing relative displacements of the two enantiomers comprising the  $[\mu\text{HSH}]_2$  dimer. Actual amplitude of this  $[\mu\text{HSH}]-[\mu\text{HSH}]_m$  vibration is  $\sim 0.05\text{ \AA}$ . (B) Low-frequency ( $<350\text{ cm}^{-1}$ )  $^{57}\text{Fe}$ -PVDOS spectra for the  $\mu\text{HSH}$  compound from NRVS experiment (blue) and DFT calculations using  $[\mu\text{HSH}]_2$  dimer (black) and  $\mu\text{HSH}$  monomer (orange) models; for the full-range spectra, see Fig. S10.<sup>†</sup>

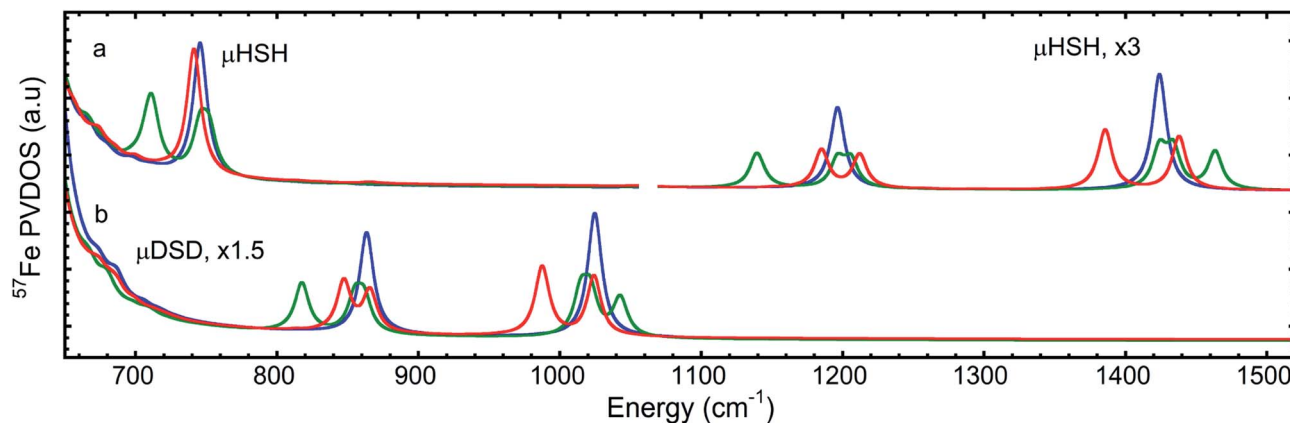


Fig. 6 DFT  $^{57}\text{Fe}$ -PVDOS spectra for the (a) H- (top) and (b) D- (bottom) isotopologues in the iron-hydride bands region  $>650\text{ cm}^{-1}$ :  $\mu\text{HSH}$  monomer (blue), averaged between the three  $\mu\text{HSH}/\mu\text{HSH}_{in}/\mu\text{HS}^-$  monomers (green), and the  $[\mu\text{HSH}]_2$  dimer (red) models. The relative intensity multiplication factors ( $\times$ ) are applied for visibility.



$\sim 0.01$  Å increase in the adjacent Fe–S bond length (Table S1†). This sensitivity makes NRVS a useful structural probe, but it also means that intensity can be lost by division into multiple channels in cases of sample heterogeneity.

The DFT calculations reveal that Fe–H stretching modes are even more sensitive to variability at the Fe–S ligand than the Fe–H–Fe wag modes. In contrast to the well-defined wag mode, current S/N limitations unfortunately prevented unambiguous experimental assignments of the stretching modes. The predicted position of the lower frequency  $\text{Fe}_p\text{--H}$  stretch mode is especially sensitive to the chemistry at the sulfur ligand adjacent to  $\text{Fe}_p$ , varying by almost  $70\text{ cm}^{-1}$  in the range of the considered alternatives ( $\text{S}^-$ :  $1138\text{ cm}^{-1}$ ,  $\text{SH}_{\text{out}}$ :  $1195\text{ cm}^{-1}$ ,  $\text{SMe}_{\text{in}}$ :  $1204\text{ cm}^{-1}$ ,  $\text{SH}_{\text{in}}$ :  $1206\text{ cm}^{-1}$ ).

Another result from the DFT calculations is the inequitable sharing of the bridging hydride. This is most directly seen in the optimized  $\sim 0.1$  Å Fe–H distance differences. Similar differences have been predicted by DFT previously in the bimetallic cofactors of [FeFe] and [NiFe] hydrogenases and their models.<sup>11,20,32</sup> The difference in  $\text{Fe}_{p/d}\text{--}\mu\text{H}$  bonding is also reflected in the prediction of two distinct Fe–H stretching modes split by as much as  $322\text{ cm}^{-1}$ . Even greater asymmetry was observed in a Ni– $\mu\text{H}$ –Fe model complex, where Ni–H and Fe–H stretches were seen respectively at  $954\text{ cm}^{-1}$  and  $1468/1532\text{ cm}^{-1}$ , the latter split by  $64\text{ cm}^{-1}$  due to a conformational heterogeneity in the  $\mu\text{-pdt}$  ligand.<sup>11</sup> It is noteworthy that the asymmetry is modulated by the status of the iron-bound sulfur – a larger asymmetry occurs when the sulfur is deprotonated.

The model studies have relevance to proposed [FeFe] hydrogenase intermediates. A terminal hydride state  $\text{H}_{\text{hyd}}$  has been convincingly assigned using NRVS.<sup>18–20,29</sup> However, bridging hydride species have also been proposed for intermediates named H(s)red using other methods,<sup>29,37</sup> and a recent report has investigated the Hred state using a combination of  $^{57}\text{Fe}$ -NRVS and other spectroscopies, supported by QM/MM calculations.<sup>29</sup> It was proposed that the Hred state contains a bridging  $\text{Fe}_p\text{--}\mu\text{H}^- \text{--Fe}_d$  hydride with its wag distributed among the  $\sim 600\text{--}650\text{ cm}^{-1}$  (Fe–)CO/CN<sup>-</sup>/ADT motions, thus prohibiting its direct observation.

Our experimental results on model compounds found wagging modes at higher frequencies, ranging from  $694\text{--}702\text{ cm}^{-1}$  in a sterically congested diiron hydride<sup>32</sup> to  $733\text{--}745\text{ cm}^{-1}$  for the current samples to  $758\text{ cm}^{-1}$  in a Ni– $\mu\text{H}$ –Fe model complex.<sup>11</sup> Of course, structural differences can conspire to move wagging modes to lower frequencies – in a recent study of a complex with an  $\text{Fe}(\mu\text{-H})_2\text{Fe}$  core the wagging modes were identified at  $455$  and  $587\text{ cm}^{-1}$ , mostly screened by other NRVS bands.<sup>38</sup> For future work with improved S/N, observation of Fe–D and Fe–H stretching modes would be a more rigorous way to test various structural hypotheses.

## Summary and outlook

In this work we have characterized the  $\mu\text{HSH}$  and  $\mu\text{HSMe}$  (and likely  $\mu\text{HS}^-$ ) synthetic models with NRVS experiments and DFT calculations. Foremost, we have directly identified the well-separated Fe–H–Fe wagging modes both in the experimental

and DFT-simulated spectra. The related Fe–D–Fe wagging modes were found to be heavily mixed with Fe–CO vibrations. The wagging mode displays significant variability that makes it a sensitive test of molecular structure.

Fe–H and Fe–D stretching modes were also scrutinized by DFT modeling for the isomeric  $\mu\text{HSH}_{\text{in/out}}$  and deprotonated  $\mu\text{HS}^-$  forms of  $\mu\text{HSH}$ , as well as a  $[\mu\text{HSH}]_2$  dimer relevant to the polycrystalline NRVS sample. These modes exhibit larger frequency and intensity shifts, making them an even more delicate probe of iron-hydride bonding. Their routine application awaits improvements in sample preparation, beamline flux, monochromators, and detectors.

## Conflicts of interest

There are no conflicts to declare.

## Acknowledgements

This work was funded by National Institutes of Health Grant GM-65440, National Science Foundation grant CHE 1308384, the Einstein Foundation Berlin grant number EVF-2016-277 (S. P. C.), the Deutsche Forschungsgemeinschaft (DFG, German Research Foundation) under Germany's Excellence Strategy – EXC 2008 – 390540038 – UniSysCat (V. P.), and the Ministry of Science and Technology of Taiwan and Academia Sinica (AS-SS-108-02-1) (Y.-C.L., M.-H.C). Some computational work was performed under the XSIM project on the CORI computing system at NERSC a U.S. Department of Energy Office of Science User Facility operated under contract no. DE-AC02-05CH11231. Synchrotron experiments were performed at SPring-8 under proposal numbers 2014A2056, 2015A0103-2016B0103, 2016A1154, 2017A1115, 2018A1409 (under JASRI) and 20150048, 20160063 (under RIKEN).

## Notes and references

- P. M. Vignais, B. Billoud and J. Meyer, *FEMS Microbiol. Rev.*, 2001, **25**, 455–501.
- P. M. Vignais and B. Billoud, *Chem. Rev.*, 2007, **107**, 4206–4272.
- W. Lubitz, H. Ogata, O. Rudiger and E. Reijerse, *Chem. Rev.*, 2014, **114**, 4081–4148.
- J. W. Peters, G. J. Schut, E. S. Boyd, D. W. Mulder, E. M. Shepard, J. B. Broderick, P. W. King and M. W. W. Adams, *Biochim. Biophys. Acta, Mol. Cell Res.*, 2015, **1853**, 1350–1369.
- D. Lukoyanov, N. Khadka, Z. Y. Yang, D. R. Dean, L. C. Seefeldt and B. M. Hoffman, *J. Am. Chem. Soc.*, 2016, **138**, 1320–1327.
- H. Ogata, K. Nishikawa and W. Lubitz, *Nature*, 2015, **520**, 571–575.
- G. F. Huang, T. Wagner, M. D. Wodrich, K. Ataka, E. Bill, U. Ermler, X. L. Hu and S. Shima, *Nat. Catal.*, 2019, **2**, 537–543.
- D. F. Harris, D. A. Lukoyanov, S. Shaw, P. Compton, M. Tokmina-Lukaszewska, B. Bothner, N. Kelleher,



- D. R. Dean, B. M. Hoffman and L. C. Seefeldt, *Biochemistry*, 2018, **57**, 701–710.
- 9 D. F. Harris, D. A. Lukoyanov, H. Kallas, C. Trncik, Z. Y. Yang, P. Compton, N. Kelleher, O. Einsle, D. R. Dean, B. M. Hoffman and L. C. Seefeldt, *Biochemistry*, 2019, **58**, 3293–3301.
- 10 D. Schilter, J. M. Camara, M. T. Huynh, S. Hammes-Schiffer and T. B. Rauchfuss, *Chem. Rev.*, 2016, **116**, 8693–8749.
- 11 H. Ogata, T. Krämer, H. Wang, D. Schilter, V. Pelmeshnikov, M. van Gastel, F. Neese, T. B. Rauchfuss, L. B. Gee, A. D. Scott, Y. Yoda, Y. Tanaka, W. Lubitz and S. P. Cramer, *Nat. Commun.*, 2015, **6**, 7890.
- 12 Y. Ohki, *Bull. Chem. Soc. Jpn.*, 2014, **87**, 1–19.
- 13 S. Ogo, *Coord. Chem. Rev.*, 2017, **334**, 43–53.
- 14 S. Rumpel, C. Sommer, E. Reijerse, C. Fares and W. Lubitz, *J. Am. Chem. Soc.*, 2018, **140**, 3863–3866.
- 15 J. A. Denny and M. Y. Darensbourg, *Chem. Rev.*, 2015, **115**, 5248–5273.
- 16 N. A. Arnet, N. Bhuvanesh and M. Y. Darensbourg, *J. Biol. Inorg. Chem.*, 2019, **24**, 909–917.
- 17 J. F. Duan, M. Senger, J. Esselborn, V. Engelbrecht, F. Wittkamp, U. P. Apfel, E. Hofmann, S. T. Stripp, T. Happe and M. Winkler, *Nat. Commun.*, 2018, **9**, 4726.
- 18 C. C. Pham, D. W. Mulder, V. Pelmeshnikov, P. W. King, M. W. Ratzloff, H. Wang, N. Mishra, E. E. Alp, J. Zhao, M. Y. Hu, K. Tamasaku, Y. Yoda and S. P. Cramer, *Angew. Chem. Int. Ed.*, 2018, **57**, 10605–10609.
- 19 E. J. Reijerse, C. C. Pham, V. Pelmeshnikov, R. Gilbert-Wilson, A. Adamska-Venkatesh, J. F. Siebel, L. B. Gee, Y. Yoda, K. Tamasaku, W. Lubitz, T. B. Rauchfuss and S. P. Cramer, *J. Am. Chem. Soc.*, 2017, **139**, 4306–4309.
- 20 V. Pelmeshnikov, J. A. Birrell, C. C. Pham, N. Mishra, H. X. Wang, C. Sommer, E. Reijerse, C. P. Richers, K. Tamasaku, Y. Yoda, T. B. Rauchfuss, W. Lubitz and S. P. Cramer, *J. Am. Chem. Soc.*, 2017, **139**, 16894–16902.
- 21 D. W. Mulder, Y. Guo, M. W. Ratzloff and P. W. King, *J. Am. Chem. Soc.*, 2017, **139**, 83–86.
- 22 W. Dong, M. Wang, X. Liu, K. Jin, G. Li, F. Wang and L. Sun, *Chem. Commun.*, 2006, 305–307, DOI: 10.1039/B513270C.
- 23 S. Ezzaher, A. Gogoll, C. Bruhn and S. Ott, *Chem. Commun.*, 2010, **46**, 5775–5777.
- 24 Y.-C. Liu, K.-T. Chu, Y.-L. Huang, C.-H. Hsu, G.-H. Lee, M.-C. Tseng and M.-H. Chiang, *ACS Catal.*, 2016, **6**, 2559–2576.
- 25 U.-P. Apfel, D. Troegel, Y. Halpin, S. Tschierlei, U. Uhlemann, H. Görls, M. Schmitt, J. Popp, P. Dunne, M. Venkatesan, M. Coey, M. Rudolph, J. G. Vos, R. Tacke and W. Weigand, *Inorg. Chem.*, 2010, **49**, 10117–10132.
- 26 T. Petrenko, W. Sturhahn and F. Neese, *Hyperfine Interact.*, 2007, **175**, 165–174.
- 27 W. R. Scheidt, J. F. Li and J. T. Sage, *Chem. Rev.*, 2017, **117**, 12532–12563.
- 28 L. B. Gee, H. X. Wang and S. P. Cramer, in *Fe-S Cluster Enzymes, Part B*, ed. S. S. David, Academic Press, Cambridge, MA, 1st edn, 2018, vol. 599, ch. 14, pp. 409–425.
- 29 S. Mebs, J. Duan, F. Wittkamp, S. T. Stripp, T. Happe, U.-P. Apfel, M. Winkler and M. Haumann, *Inorg. Chem.*, 2019, **58**, 4000–4013.
- 30 J. Birrell, V. Pelmeshnikov, N. Mishra, H. Wang, Y. Yoda, K. Tamasaku, T. B. Rauchfuss, S. P. Cramer, W. Lubitz and S. DeBeer, *J. Am. Chem. Soc.*, 2020, **142**, 222–232.
- 31 V. Pelmeshnikov, L. B. Gee, H. Wang, K. C. MacLeod, S. F. McWilliams, K. L. Skubi, S. P. Cramer and P. L. Holland, *Angew. Chem., Int. Ed.*, 2018, **57**, 9367–9371.
- 32 M. R. Carlson, D. L. Gray, C. P. Richers, W. Wang, P.-H. Zhao, T. B. Rauchfuss, V. Pelmeshnikov, C. C. Pham, L. B. Gee, H. Wang and S. P. Cramer, *Inorg. Chem.*, 2018, **57**, 1988–2001.
- 33 K. Nakamoto, *Infrared & Raman Spectra of Inorganic & Coordination Compounds*, Wiley-Interscience, New York, 5th edn, 1997.
- 34 Y. C. Liu, K. T. Chu, R. L. Jhang, G. H. Lee and M. H. Chiang, *Chem. Commun.*, 2013, **49**, 4743–4745.
- 35 Y. Xiao, H. Wang, S. J. George, M. C. Smith, M. W. W. Adams, J. F. E. Jenney, W. Sturhahn, E. E. Alp, J. Zhao, Y. Yoda, A. Dey, E. I. Solomon and S. P. Cramer, *J. Am. Chem. Soc.*, 2005, **127**, 14596–14606.
- 36 Y. Xiao, M.-L. Tan, T. Ichiye, H. Wang, Y. Guo, M. C. Smith, J. Meyer, W. Sturhahn, E. E. Alp, J. Zhao, Y. Yoda and S. P. Cramer, *Biochemistry*, 2008, **47**, 6612–6627.
- 37 P. Chernev, C. Lambertz, A. Brunje, N. Leidel, K. G. V. Sigfridsson, R. Kositzki, C. H. Hsieh, S. L. Yao, R. Schiwon, M. Driess, C. Limberg, T. Happe and M. Haumann, *Inorg. Chem.*, 2014, **53**, 12164–12177.
- 38 V. Pelmeshnikov, L. B. Gee, H. Wang, K. C. MacLeod, S. F. McWilliams, K. L. Skubi, S. P. Cramer and P. L. Holland, *Angew. Chem., Int. Ed.*, 2018, **130**, 9511–9515.

